Spectroscopic Characterization of Cobalt-Containing Mesoporous Materials

Torbjørn Vrålstad,*,† Wilhelm R. Glomm,† Magnus Rønning,‡ Hendrik Dathe,§ Andreas Jentys,§ Johannes A. Lercher,§ Gisle Øye,† Michael Stöcker,# and Johan Sjöblom†

Ugelstad Laboratory, Department of Chemical Engineering, Norwegian University of Science and Technology (NTNU), N-7491 Trondheim, Norway, Department of Chemical Engineering, Norwegian University of Science and Technology (NTNU), N-7491 Trondheim, Norway, Department of Chemistry, Technical University Munich (TUM), D-85747 Garching, Germany, and SINTEF Materials and Chemistry, P.O. Box 124 Blindern, N-0314 Oslo, Norway

Cobalt-containing mesoporous materials that have been prepared using different procedures have been comparatively characterized by transmission electron microscopy/energy-dispersive X-ray spectroscopy (TEM/EDS), extended X-ray absorption fine structure spectroscopy (EXAFS), X-ray absorption near edge spectroscopy (XANES), and ultraviolet−visible (UV−vis), near-infrared (NIR), and mid-infrared (mid-IR) spectroscopies, and the results provide new insights into the local environment and properties of cobalt in this type of material. TEM/EDS analyses have shown that tetraethyl orthosilicate (TEOS) may be less appropriate as a silicon source during the syntheses of cobalt-containing mesoporous materials, because the distribution of cobalt throughout the framework may become uneven. EXAFS has been determined to be the most suitable method for direct verification of framework incorporation, by identifying silicon as the backscatterer in the second shell. Such a direct verification may not be obtained using UV−vis spectroscopy. From EXAFS analyses, it is also possible to distinguish between surface-bound and framework-incorporated cobalt. There is a good agreement between the results obtained from XANES and UV−vis regarding the coordination symmetry of cobalt in the samples. The presence of cobalt in the silica framework has been determined to create Lewis acid sites, and these acid sites are suggested to be located at tetrahedral cobalt sites at the surface.

1. Introduction

Cobalt-containing microporous materials are active as catalysts in several different reactions, such as the selective catalytic reduction of NO_x.[1−3] Spectroscopic methods such as X-ray absorption, ultraviolet−visible (UV−vis) spectroscopy, and infrared (IR) spectroscopy are routinely used to characterize the nature and local environment of the cobalt sites in these types of materials,[4−11] as well as to study changes during reduction/oxidation.[12−15] Therefore, extensive information about cobalt-containing microporous materials has been obtained, and some reviews on spectroscopy and coordination chemistry in these materials have been published.[16,17]

However, the local environment of cobalt incorporated into mesoporous materials is somewhat different than for cobalt in microporous materials. Unlike the crystalline zeolites and zeotypes, the mesoporous silica materials have an amorphous wall structure and thicker pore walls,[18,19] which should create a different local environment around incorporated metals and perhaps lead to different findings from spectroscopic characterization methods. Cobalt-containing mesoporous materials have previously been studied using several spectroscopic methods for objectives such as routine characterization,[20−26]

verification of framework incorporation,[25,27] and determination of oxidation state and local environment during reduction.[28,29] To our knowledge, however, no comparative studies of the obtainable information from the different spectroscopic methods have yet been reported for mesoporous materials.

We have incorporated cobalt into or onto the silica framework of mesoporous materials by different methods, and here, we report, a comparative characterization of these samples by transmission electron microscopy/energy-dispersive X-ray spectroscopy (TEM/EDS), extended X-ray absorption fine structure (EXAFS), X-ray absorption near edge spectroscopy (XANES), UV−vis, near-infrared (NIR), and mid-infrared (mid-IR), with an emphasis on verification of framework incorporation and how this incorporation may affect the property of the materials.

2. Experimental Section

Chemicals. Cetyl trimethylammonium bromide (CTAB) and tetraethyl orthosilicate (TEOS, 98%) were purchased from Acros. 3-(2-Aminoethylamino)propyltrimethoxysilane (>98%) was purchased from Fluka. NaOH (>99%), Co(Ac)$_2$·4H$_2$O (>99%), CoCl$_2$·6H$_2$O (>99%), Co(NO$_3$)$_2$·6H$_2$O (>99%) were purchased from Merck. The sodium silicate solution (27% SiO$_2$, 10% NaOH) was purchased from Riedel-de Haën, and H$_2$SO$_4$ (95%) was purchased from Prolabo. Ethanol was purchased from Arcus, and toluene was obtained from Lab Scan. All chemicals were used as received.

Synthesis of MCM-41. Sample MCM-41 was prepared using the procedure reported by Beck et al.[19] A quantity (32.8 g) of CTAB was dissolved in 168 g of deionized water during stirring. When a clear solution was obtained, 3.0 g of H$_2$SO$_4$ (50%) was

　* Author to whom correspondence should be addressed. Tel.: +47 73 55 03 39. Fax: +47 73 59 40 80. E-mail address: torbjorn.vralstad@chemeng.ntnu.no.

　† Ugelstad Laboratory, Department of Chemical Engineering, Norwegian University of Science and Technology (NTNU).

　‡ Department of Chemical Engineering, Norwegian University of Science and Technology (NTNU).

　§ Department of Chemistry, Technical University Munich.

　# SINTEF Materials and Chemistry.

Cobalt-Containing Mesoporous Materials

J. Phys. Chem. B, Vol. 110, No. 11, 2006 **5387**

added dropwise. Then, 43.6 g of sodium silicate (27% SiO_2, 10% NaOH) was added, and a white gel was immediately precipitated. The gel solution was transferred into a Teflon bottle and heated under static conditions at 100 °C for 6 days. The precipitate was then filtered, washed several times with deionized water, dried overnight at room temperature, and calcined at 550 °C for 7 h in air. The molar composition of the synthesis gel was as follows: $CTAB:Na_2Si_3O_7:H_2O:H_2SO_4$ = 1:2:104: 0.09.

Incorporation of Cobalt. Cobalt was incorporated into the framework of MCM-48 and MCM-41 by direct, "one-pot" procedures. More details of these procedures have been reported elsewhere, as cited below.

Co−MCM-41, Procedure A.[30] $CoCl_2\cdot6H_2O$ (0.3 g) and 21.1 g CTAB were dissolved in 67.5 g of deionized water. Seventeen grams of ethanol (96%) were added and stirred for 30 min. A quantity (20.5 g) of sodium silicate (27% SiO_2, 10% NaOH) was dissolved in 20.5 g of deionized water and added to the surfactant solution, which resulted in the precipitation of a blue gel. The gel solution was stirred for 30 min, and transferred to a Teflon bottle and heated under static conditions at 100 °C for 72 h. The precipitate was then treated as for MCM-41 above. Molar composition of the gel: $CTAB:Na_2Si_3O_7:EtOH:CoCl_2:$ H_2O = 1:1.46:6.37:0.022:84.4. This sample has been denoted OP-41-A, where "OP" is an abbreviation of "one-pot".

Co−MCM-41, Procedure B.[25] CTAB (21.9 g) was dissolved in 116.5 g of deionized water, and stirred until a clear solution was obtained. A quantity (1.26 g of $Co(NO_3)_2\cdot6H_2O$) was dissolved in 10 g of deionized water and added dropwise to the surfactant solution. Sodium silica ($Na_2Si_3O_7$, 27% SiO_2) (29 g) was diluted to 29 g of deionized water and added to the red cobalt/surfactant solution, resulting in the precipitation of a blue gel. The gel solution was transferred to a Teflon bottle and heated under static conditions at 100 °C for 6 days. The precipitate was then treated as for MCM-41 above. Molar composition of the synthesis gel was as follows: $CTAB:Na_2$-$Si_3O_7:Co(NO_3)_2:H_2O$ = 1:2:0.07:162. This sample has been denoted OP-41-B.

Co−MCM-48.[25] A quantity of $CoCl_2\cdot6H_2O$ (0.90 g) and 31.6 g of CTAB were dissolved in 83.4 g of deionized water and stirred until a clear solution was obtained. A small amount (2.68 g) of NaOH and 28.9 g of TEOS were dissolved in 68 g of deionized water, and stirred for 5 min. This solution was then added to the surfactant solution, and a blue gel was precipitated during stirring for 15 min. The gel solution was then transferred to a Teflon bottle and heated under static conditions at 100 °C for 72 h. The precipitate was then treated in the same manner as for MCM-41 previously. The molar composition was as follows: $CTAB:TEOS:CoCl_2:NaOH:H_2O$ = 1:1.6:0.05:0.8:97. This sample has been denoted OP-48.

Surface Grafting of Cobalt. For comparison, cobalt was grafted at the surface of MCM-41 by organosilane molecules, in a post-synthesis procedure. More details of this and similar experiments are reported elsewhere.[31] 3-(2-Aminoethylamino)-propyltrimethoxysilane (5.0 mL) was added to 1.0 g MCM-41 in 50 mL of toluene and refluxed under a nitrogen atmosphere for 10 h. The solution was filtered, washed with toluene, and then washed thoroughly with ethanol. $Co(Ac)_2\cdot4H_2O$ (0.26 g) was dissolved in 50 mL of ethanol, and the silica material was added to this solution, which was then stirred for 12 h. The solution was filtered, washed with ethanol, and then washed thoroughly with water. After drying at room temperature overnight, the sample was calcined at 600 °C to remove all

organic materials. This sample has been denoted G-41, where the symbol "G" represents grafting.

Characterization. X-ray diffraction (XRD) data were collected on a Siemens model D-5005 instrument with Cu Kα radiation, with a step length of 0.03° (2θ) and a step time of 6 s. inductively coupled plasma−atomic emission spectrophotometry (ICP−AES) was performed using a Jarrell Ash Thermo Iris Advantage instrument. A small amount (0.1 g) of sample was dissolved in 5 mL of concentrated HCl; the resulting solution was then diluted with distilled water to 50 mL and measured for cobalt content. X-ray fluorescence (XRF) data were collected on a Bruker model axs S4 PIONER instrument. The samples were mixed with wax and pressed into pellets before analysis. TEM images and subsequent EDS analyses were obtained using a JEOL model 2010 F instrument. The samples were placed on a copper mesh sample grid and were prepared by dispersing the powder in deionized water using an ultrasonic bath. The nominal probe size of the EDS was ∼1 nm.

X-ray absorption spectroscopy (XAS) data were collected at the Swiss-Norwegian Beamlines (SNBL) at the European Synchrotron Radiation Facility (ESRF) in Grenoble, France. The data were collected at the Co K-edge (7709 eV) in transmission mode in room temperature, and a channel-cut Si(111) monochromator was used to obtain the data. Higher-order harmonics were rejected by means of a gold-coated mirror that was angled at 7.3 mrad, with respect to the beam. The EXAFS data were summed, background-subtracted, and converted to *k*-space using the WinXAS program,[32] and the least-squares curve fitting was performed by the EXCURVE 98 program,[33] based on single-scattering, curved-wave theory with k^3-weighting and ab initio phase shifts, as calculated by the program. The XANES profiles were analyzed using the WinXAS program.[32]

UV−vis spectra were collected using a Shimadzu model UV-2401 PC instrument with an ISR-240A Integrating Sphere Attachment operating in reflectance mode. Diffuse reflectance near-infrared (NIR) spectra were collected using a Bruker Optics Multi-Purpose Analyzer with an Integrating Sphere Attachment. Mid-infrared (IR) spectra were obtained using a Perkin−Elmer model 2000-FTIR instrument that was equipped with a vacuum cell. The samples were pressed into self-supported wafers (*d* = 12 mm, weight = 4−5 mg), and the spectra were collected after activation at 450 °C (increment of 10 °C/min) for 60 min in a vacuum of <10^{-6} mbar. The type and strength of acid sites were determined by the adsorption of pyridine at 150 °C with a partial pressure of 10^{-2} mbar, while collecting IR spectra. The spectra were normalized using the integral hydroxyl groups intensity of the bands assigned to the structural vibrations of MCM-41 between 2100 and 1770 cm^{-1}, as described by Jentys et al.[34] The concentration of hydroxyl group (acidity) was calculated by a method based on the molar extinction coefficients reported by Emeis.[35]

3. Results and Discussion

An overview of the different samples tested in this work is presented in Table 1. Figure 1 shows XRD patterns of samples OP-41-A, OP-41-B, OP-48, and G-41, all of which display diffraction peaks that are characteristic for mesoporous materials.[18,19] The results obtained from these samples will be presented and discussed according to characterization method.

Transmission Electron Microscopy/Energy-Dispersive Spectroscopy (TEM/EDS). Although TEM is, in principle, not a spectroscopic method, the electron beam generates X-ray fluorescence radiation as it passes through the sample, and from these EDS spectra it is possible to detect and quantify the

TABLE 1: Overview of Some Properties of the Different Samples Tested

sample	cobalt content (wt %)	structure[a]	location of Co	color
OP-41-A (calc)	4.1[b]	hexagonal	framework	blue-gray
OP-41-B (calc)	4.7[b]	hexagonal	framework	gray
OP-48 (calc)	3.8[b]	cubic *Ia3d*	framework	gray
G-41	4.8[c]	hexagonal	surface	blue
OP-41-A as-synth	not measured	hexagonal	framework	purple-pink
OP-41-B as-synth	not measured	hexagonal	framework	purple-pink

[a] Determined by XRD (see Figure 1). [b] Measured by XRF. [c] Measured by ICP−AES.
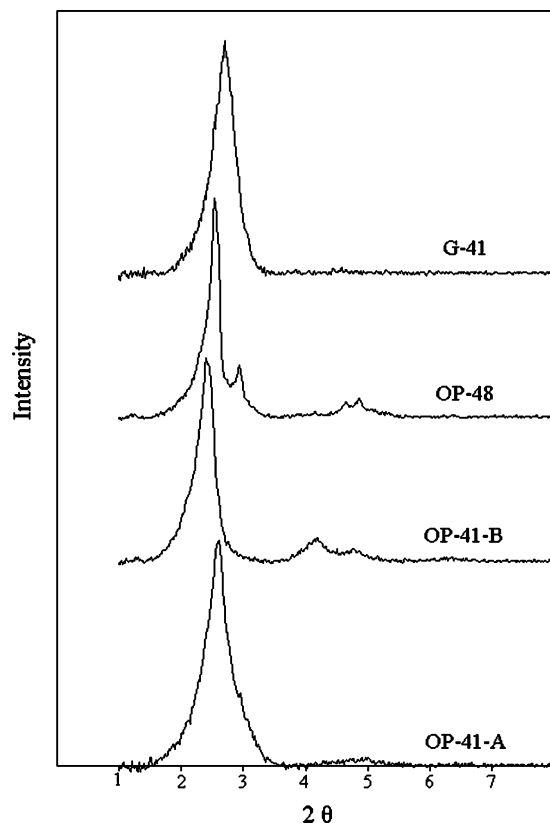
Figure 1. Low-angle X-ray diffraction (XRD) patterns of samples OP-41-A, OP-41-B, OP-48, and G-41.

different elements in the sample. Figure 2 shows a TEM image of sample OP-41-A with two EDS spectra taken from different regions, which are representative for the entire sample. The EDS spectra show that silicon, oxygen, and cobalt are present in equal amounts in both regions, i.e., the cobalt is homogeneously dispersed throughout the sample. Sample OP-41-B also displays a similar TEM/EDS profile (data not shown).

A TEM image of sample OP-48 with two EDS spectra taken from different representative regions is shown in Figure 3. The EDS spectra show that some parts of this sample actually do not contain any cobalt at all, i.e., the cobalt is not incorporated homogeneously into the framework throughout the entire sample. Although this sample has a cubic *Ia3d* structure (see Figure 1) and the cobalt content is 3.8 wt % (see Table 1), it might therefore actually be misleading to call this sample Co-MCM-48, as the cobalt is only incorporated into parts of the sample. This uneven distribution of cobalt may be caused by the organic nature of the silica source in this sample (TEOS). Because of the slow hydrolysis of TEOS, all the cobalt in the gel may be incorporated into the hydrolyzed silica while some TEOS is still not hydrolyzed. This TEOS will later form the cobalt-free framework, thus causing the uneven cobalt distribu-

tion that is observed in Figure 3. Therefore, these results indicate that inorganic silica sources, which are already hydrolyzed and react fast, should be used in the synthesis of metal-containing mesoporous materials when a uniform distribution of the metal is desired. Because of this uneven cobalt distribution, we will not discuss sample OP-48 in any more detail throughout this work.

TEM/EDS analyses of sample G-41 show that the cobalt was unevenly distributed in this sample as well (data not shown). This is probably due to the poor wetting ability of the nonpolar toluene on the polar silica surface combined with the small pores of MCM-41, which cause an uneven dispersion of organosilane molecules on the internal silica surface during the grafting procedure and, thus, an uneven distribution of cobalt on the calcined G-41 sample.

Extended X-ray Absorption Fine Structure (EXAFS). EXAFS is a powerful method for studying the structure of materials, because it provides information about the local environment of selected elements in the samples in question.[36] The EXAFS signal in the absorption spectrum is caused by the interference between the emitted electron wave and the electron waves that are backscattered from neighboring atoms. Through theoretical least-squares curve fitting, the distance to these backscattering neighbors may be determined, as well as their multiplicity and identity. Figure 4 shows the Co K-edge k^3-weighted $\chi(k)$ curves and the respective Fourier transforms of the model compounds Co-foil, Co_3O_4, CoO, and $Co(OH)_2$. The results of the EXAFS curve fitting for these samples are listed in Table 2, and it is evident from both Figure 4 and Table 2 that the local environment of cobalt is very different in these four materials.

Because of the possibility of determining the distance to and type of neighboring atoms, EXAFS is a well-suited method for providing a direct verification of the incorporation of metals such as cobalt into the framework of mesoporous materials. Perhaps the most crucial element in this verification is the identification of the neighboring atoms, which should be O in the first shell and Si in the second shell, if Co is incorporated into the framework by replacing Si. Figure 5 shows the Co K-edge k^3-weighted $\chi(k)$ curves and the respective Fourier transforms of the as-synthesized and calcined sample OP-41-A and sample G-41, and Table 3 lists the results of the EXAFS curve fitting for these samples and also of as-synthesized and calcined sample OP-41-B. (Note that the curve-fitting results of sample OP-41-B have been previously published.[25]) Oxygen is identified as the backscatterer in the first shell for all these samples. There is a decrease in the multiplicity of this shell during calcination from ~5 to ~4 for both OP samples, which is probably caused by the removal of surface-bound water. There is also a slight reduction in the interatomic distance from the Co atoms to the O atoms during calcination, which is an indication of lattice contraction. The coordination number of sample G-41 is also ~4; however, the distance to the O atoms is less than that in the OP samples.

However, perhaps more important than the first shell is the second backscattering shell. Oxygen is also the first backscatterer of both cobalt oxides and of cobalt hydroxide (see Table 2), so an analysis of the first shell only will not provide any direct verification of framework incorporation. Table 3 shows that silicon is identified as the backscatterer in the second shell for all the mesoporous samples, which verifies the incorporation of cobalt into the framework. The signal from this shell was Fourier-filtered and analyzed thoroughly, and no cobalt back-scatterers were detected, only silicon. However, the presence
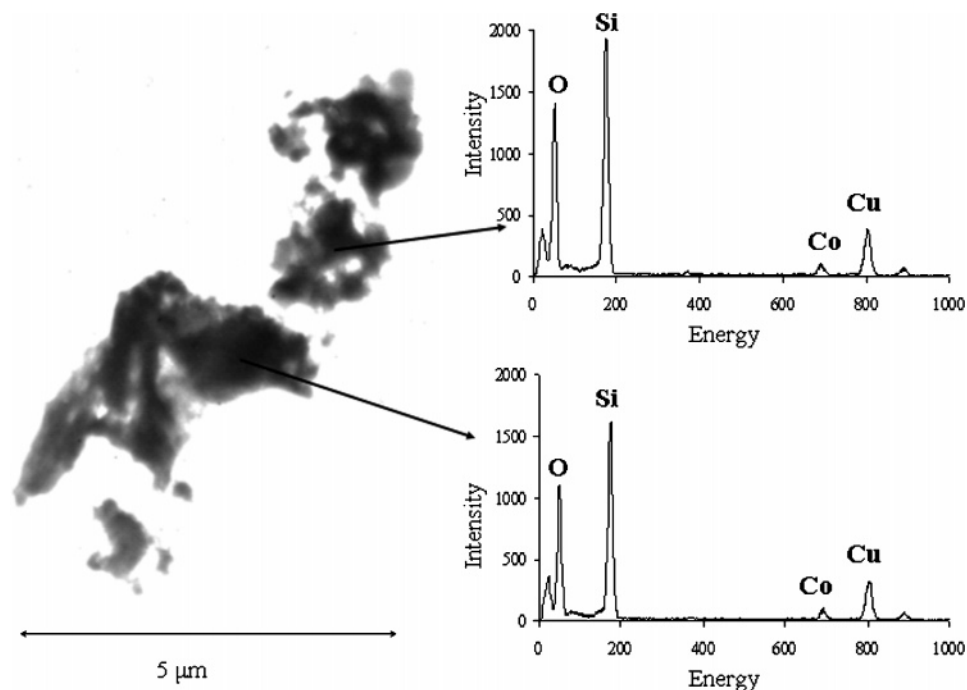
Figure 2. (Left) Transmission electron microscopy (TEM) micrograph of sample OP-41-A with (right) EDS spectra taken from two different locations. The Cu peaks in the EDS spectra are from the sample holder grid.
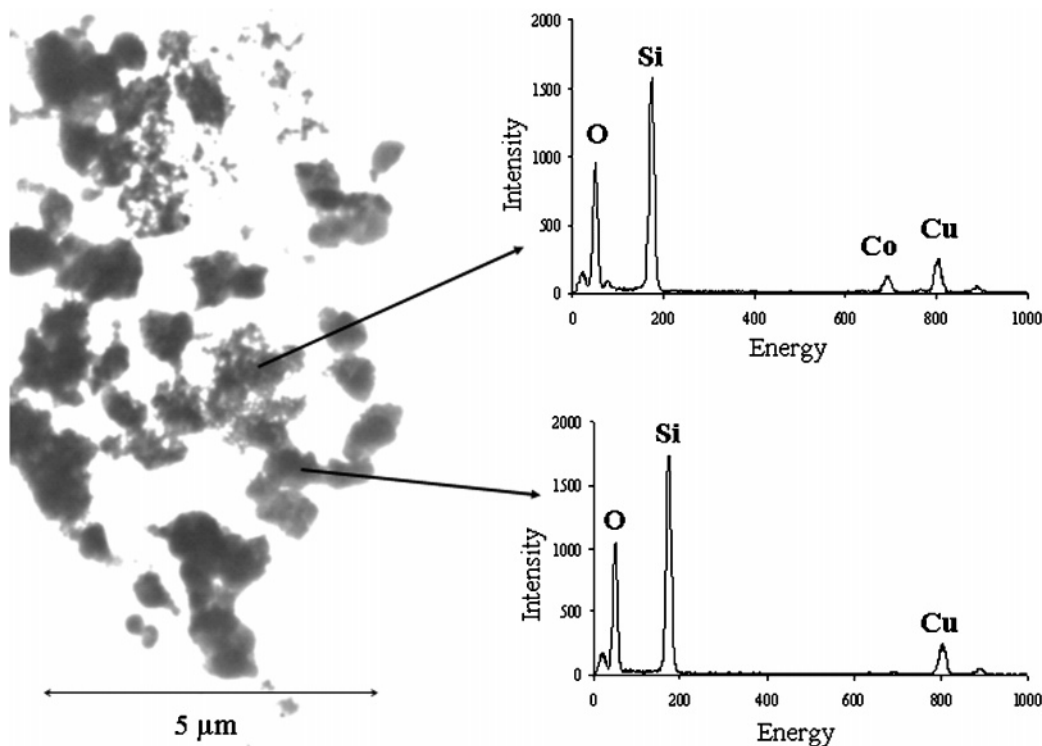

Figure 3. (Left) TEM micrograph of sample OP-48 with (right) EDS spectra taken from two different locations. The Cu peaks in the EDS spectra are from the sample holder grid.

of some cobalt in this shell cannot be completely ruled out, due to possible multiple scattering, although this is unlikely due to the amorphous nature of the pore walls. Therefore, these results show that cobalt is incorporated into the framework of the OP samples both before and after calcination, although the multiplicity of the silicon shell is decreased during calcination. This decrease is probably caused by a partial breakdown of the framework due to the low thermal stability of cobalt-containing mesoporous samples.[25] The multiplicity of the silicon shell for the G-41 sample is only 1.4 (Table 3), which is significantly

lower than for the OP samples. This low multiplicity is no surprise, because the cobalt is located at the framework surface in sample G-41, not inside the framework, as for the OP samples. The Co···Si distance is also shorter for the G-41 sample than for the OP samples. These results indicate that by careful EXAFS analyses it could be possible to distinguish between surface-bound and framework-incorporated cobalt.

This distinction between surface-bound and framework-incorporated cobalt might also explain one of the differences between the EXAFS results for mesoporous materials presented
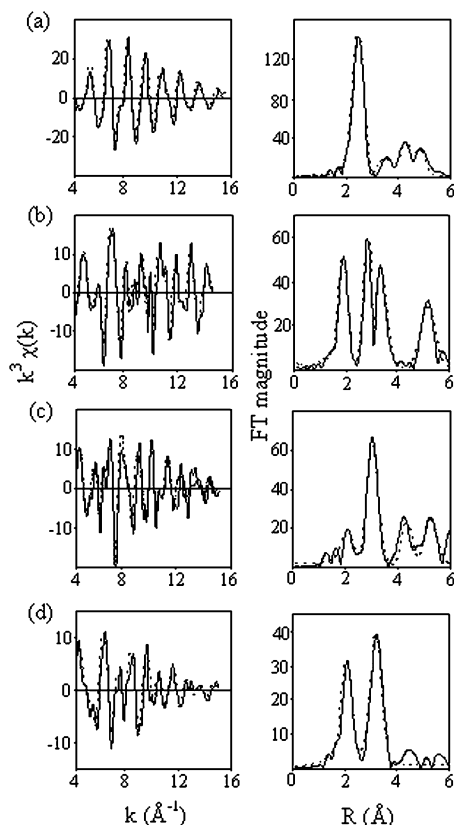
Figure 4. (Left) k^3-weighted $\chi(k)$ curves and (right) Fourier transforms of the Co K-edge of the model compounds: (a) Co-foil, (b) Co_3O_4, (c) CoO, and (d) $Co(OH)_2$. The experimental curve is represented by the solid line, and the theoretical curve is represented by the dashed line.

TABLE 2: Results of EXAFS Curve Fitting for the Model Compounds

shell	N^a	R (Å)^b	$2\sigma^2$(Å^2)^{b,c}
	Co-foil		
Co−Co	12.0	2.497(1)	0.0115(5)
Co···Co	6.0	3.536(9)	0.018(2)
Co···Co	18.0	4.368(6)	0.017(1)
Co···Co	12.0	4.851(6)	0.011(1)
	Co_3O_4		
Co−O	1.33	1.90(2)	0.002(1)
Co−O	4.0	1.93(1)	0.006(1)
Co···Co	4.0	2.858(3)	0.0048(6)
Co···Co	8.0	3.368(4)	0.0108(9)
Co···Co	8.0	5.00(1)	0.009(2)
Co···Co	10.66	5.32(1)	0.010(2)
	CoO		
Co−O	6.0	2.11(1)	0.017(3)
Co···Co	12.0	3.006(3)	0.0146(8)
Co···Co	6.0	4.345(9)	0.009(2)
Co···Co	24.0	5.236(9)	0.019(2)
	$Co(OH)_2$		
Co−O	6.0	2.093(4)	0.013(1)
Co···Co	6.0	3.164(3)	0.0140(7)

^{a} Multiplicity of backscatter. ^{b} Uncertainties in the last digit are given in parentheses. ^{c} σ is the Debye−Waller type factor.

here and previously reported EXAFS results for microporous materials: The EXAFS signal from metal-containing microporous materials is usually dominated by the signal from the first shell, i.e., oxygen.[12,13,15] There are very weak signals from the backscatterers in the second shell, which are silicon for zeolites and aluminum or phosphorus for AlPO's. The curve fitting of the EXAFS signal from microporous materials is therefore often limited to the oxygen shell only. This is probably
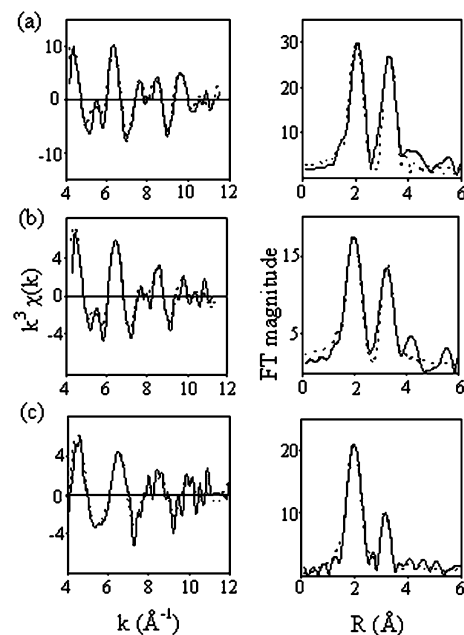

Figure 5. (Left) k^3-weighted $\chi(k)$ curves and (right) Fourier transforms of the Co K-edge of (a) as-synthesized sample OP-41-A, (b) calcined sample OP-41-A, and (c) sample G-41. The experimental curve is represented by the solid line, and the theoretical curve is represented by the dashed line.

TABLE 3: Results of EXAFS Curve Fitting for As-Synthesized and Calcined Samples OP-41-A and OP-41-B and Sample G-41

shell	N^a	R (Å)^b	$2\sigma^2$ (Å^2)^{b,c}
	Sample OP-41-A, as-synth		
Co−O	5.2	2.075(4)	0.011(2)
Co···Si	6.3	3.296(4)	0.009(2)
	Sample OP-41,-A calc		
Co−O	4.3	2.019(5)	0.018(1)
Co···Si	4.4	3.251(5)	0.014(1)
	Sample OP-41-B, as-synth		
Co−O	4.9	2.073(3)	0.0096(9)
Co···Si	6.9	3.297(3)	0.0091(9)
	Sample OP-41-B, calc		
Co−O	4.0	2.055(4)	0.013(1)
Co···Si	6.3	3.275(4)	0.014(1)
	Sample G-41		
Co−O	4.2	2.007(4)	0.017(2)
Co···Si	1.4	3.20(1)	0.007(4)

^{a} Multiplicity of backscatter. ^{b} Uncertainties in the last digit are given in parentheses. ^{c} σ is the Debye−Waller type factor.

due to the relatively thin pore walls of microporous materials, which are normally only a few angstroms thick. Most of the incorporated metals will then necessarily be located at or near the framework surface, with very few neighbors in the second backscattering shell. Mesoporous materials, on the other hand, have significantly thicker pore walls: M41S-materials are reported to have wall thicknesses of ∼10−15 Å, and SBA-materials are reported to have wall thicknesses of ∼30−60 Å.[37] These thicker pore walls provide more backscattering neighbors for incorporated metals and, thus, a stronger EXAFS signal from the second backscattering shell, as seen in Figure 5 and Table 3.

X-ray Absorption Near Edge Spectroscopy (XANES). XANES is a method that is often applied to determine the oxidation state of a selected element in a sample,[25,26,29] and this methodology also is used for in situ studies.[38−40] Qualitative information about the local geometry around the chosen element
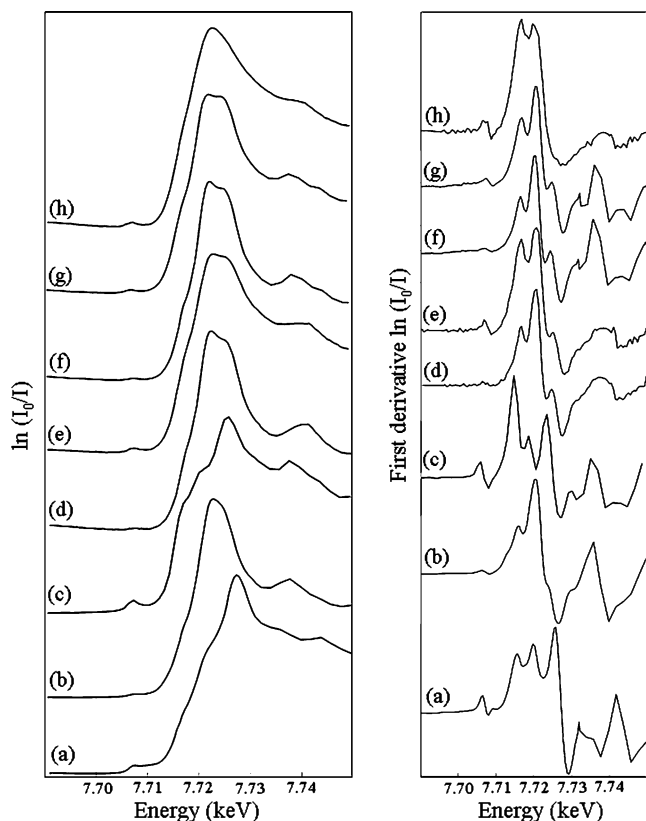
Cobalt-Containing Mesoporous Materials

J. Phys. Chem. B, Vol. 110, No. 11, 2006 **5391**

Figure 6. (Left) Normalized Co K-edge XANES profiles and (right) their first derivative for (a) Co_3O_4, (b) $Co(OH)_2$, (c) $CoAl_2O_4$, (d) as-synthesized sample OP-41-A, (e) calcined sample OP-41-A, (f) as-synthesized sample OP-41-B, (g) calcined sample OP-41-B, and (h) sample G-41.

is also obtained.[40] Figure 6 shows the Co K-edge XANES profiles and the respective first derivative of Co_3O_4, $Co(OH)_2$, as-synthesized and calcined samples OP-41-A and OP-41-B, and sample G-41. The XANES profile of model compound CoO is very similar to $Co(OH)_2$ and is not shown. A XANES profile of $CoAl_2O_4$ is also included, as it contains only tetrahedral Co-(II) and is a good reference material in this regard.

The oxidation state of a sample may be determined by looking at the position of the absorption peak, because the photon energy required to excite an electron is dependent on the oxidation state. Figure 6 shows that both the XANES profile and the first derivative are different for the two model compounds Co_3O_4 and $Co(OH)_2$, which is expected because Co_3O_4 consists of one-third Co(II) and two-thirds Co(III), whereas $Co(OH)_2$ consists of only Co(II).[41] All the XANES profiles of the mesoporous samples are similar to that of $Co(OH)_2$, which indicates that all the cobalt in these samples are present as Co(II), i.e., no cobalt in the OP samples is oxidized during calcination. However, the XANES profile, and especially the first derivative of the G-41 sample, have a slightly different line shape than the other mesoporous samples. The XANES profile of the G-41 sample and its first derivative are actually quite similar to those reported for cobalt-containing microporous materials,[8–10,15,17] which could be due to the similarity between the surface location of the cobalt in the G-41 sample and the location of cobalt in the thin pore walls of microporous materials, as discussed previously for the EXAFS results.

An important feature of the XANES profiles in Figure 6 is the small pre-edge peak, which is observed for some of the samples. This absorption peak is attributed to a 1s $\rightarrow$ 3d transition and is normally dipole-forbidden, but becomes allowed when the metal has a tetrahedral coordination. In a T_d environment, the lack of an inversion center gives the d_{xy}, d_{xz}, and d_{yz} orbitals a t_2 symmetry, which is the same symmetry as the p-orbitals. This symmetry overlap causes a mixing of these three d-orbitals and the p-orbitals,[42] which gives these d-orbitals some p-character and the 1s $\rightarrow$ 3d transition thus becomes partially dipole allowed. Therefore, the presence of such a pre-edge peak in the XANES profiles is an indication of tetrahedral coordination.

Figure 6 shows that Co_3O_4, $CoAl_2O_4$, both calcined OP samples, and sample G-41 contain pre-edge peaks, which is especially apparent from the first derivative. The model compound Co_3O_4 has the normal spinel structure, where Co-(III) occupies octahedral positions and Co(II) occupies tetrahedral positions in the FCC oxygen lattice, and these tetrahedral Co(II) cause the pre-edge peak. $CoAl_2O_4$ also has the normal spinel structure where Co occupies only tetrahedral positions, which is the cause of the strong pre-edge peak of this sample. Table 3 shows that the coordination number of both calcined OP samples and sample G-41 is ~4, which is an indication of tetrahedral local environment in these samples and is verified by the pre-edge peak in Figure 6. However, the intensity of the pre-edge peak of sample OP-41-B is lower than that for samples OP-41-A and G-41. This indicates that, although the coordination number is 4 for these three samples, there is a lower degree of tetrahedral coordination in sample OP-41-B. Despite the similar EXAFS results, the local environment of cobalt in these samples is, therefore, slightly different. Although the wall structure of mesoporous materials is amorphous, the higher degree of tetrahedral coordination in sample OP-41-A could, therefore, be an indication of a more-ordered wall structure in this sample, as compared to sample OP-41-B.

There are also small pre-edge peaks in the XANES profiles of $Co(OH)_2$ and both as-synthesized OP samples. The pre-edge peaks of the OP samples may be due to some tetrahedral cobalt inside the silica framework or they could be due to vibronic coupling, which is the cause of the pre-edge peak of the octahedral $Co(OH)_2$.[42] Because of thermal vibrations of the oxygen ligands, the inversion center in the O_h environment will temporarily disappear, and the 1s$\rightarrow$ 3d transition becomes momentarily allowed, because of the p- and d-orbital mixing previously discussed. Therefore, very small pre-edge peaks may also be observed for cobalt in octahedral coordination, as observed in Figure 6.

Ultraviolet−Visible Spectroscopy. Energy transitions in the UV−vis region are very common and are well-known to be the origin of the colors of transition-metal- containing materials. These d $\rightarrow$ d transitions are also normally dipole-forbidden, but are allowed due to the p- and d-orbital mixing that has been discussed for XANES previously. Therefore, more-intense colors are observed for tetrahedral complexes than for octahedral complexes.[42] Figure 7 shows the UV−vis spectra of as-synthesized and calcined samples OP-41-A and OP-41-B and of sample G-41. The triplet peak observed for calcined OP-41-A and G-41 is characteristic for tetrahedral Co(II) and is due to the $^4A_2 \rightarrow {}^4T_1(P)$ energy transition,[43] which causes the blue color of these samples (see Table 1). The tripartition of the peak is due to spin−orbit coupling.

Although the UV−vis spectra of these two samples are very similar, the local environment of cobalt is different in these samples, as was seen from the EXAFS results (Table 3 and Figure 5). The cobalt is incorporated into the framework of sample OP-41-A, while the cobalt is bound to the framework surface of sample G-41. Therefore, observation of this charac-
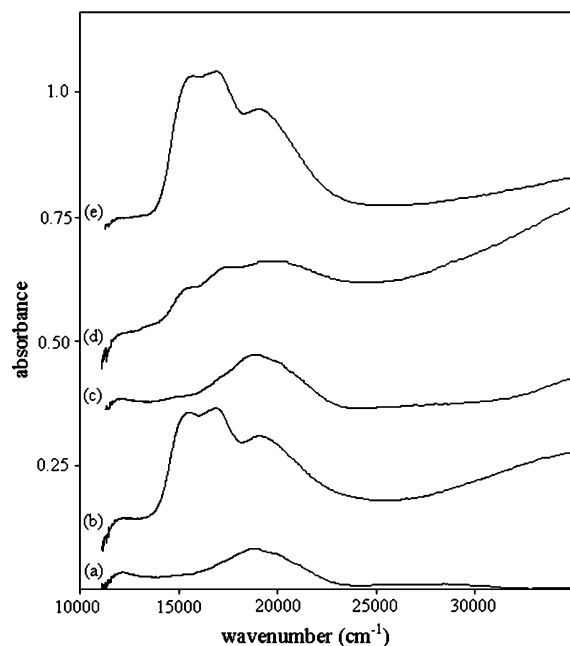
Figure 7. Ultraviolet−visible (UV−vis) spectra of (a) as-synthesized sample OP-41-A, (b) calcined sample OP-41-A, (c) as-synthesized sample OP-41-B, (d) calcined sample OP-41-B, and (e) sample G-41.

teristic Co(II) triplet in the UV−vis spectrum of a cobalt-containing mesoporous sample should not be used as a verification of framework incorporation, because the triplet only gives information about tetrahedral coordination.

This triplet is also weakly observed for the calcined sample OP-41-B, which is an indication of the presence of some tetrahedral Co(II) in this sample as well, although to a lesser degree than for calcined sample OP-41-A and sample G-41. The difference in local environment for cobalt between the two OP samples that was observed by XANES is, thus, also observable by UV−vis spectroscopy and can also be observed from the color difference between these two samples (see Table 1). Thus, there is a correlation between the intensity of the $^4A_2 \rightarrow {}^4T_1(P)$ triplet in the UV−vis region (Figure 7) and the intensity of the 1s $\rightarrow$ 3d pre-edge peak in the XANES profile (Figure 6), which should actually be expected, because both transitions are governed by the same selection rule, i.e., they are allowed because of the mixing of p- and d-orbitals in tetrahedral systems.

The color of both as-synthesized OP samples is purple-pink, which is characteristic for octahedral Co(II). This color is due to the $^4T_{1g}(F) \rightarrow {}^4T_{1g}(P)$ transition,[43] which is observed in Figure 7 for both these samples. Because of the presence of an inversion center in octahedral systems and, thus, the normally dipole-forbidden d $\rightarrow$ d transitions, this transition is only allowed due to vibronic coupling, as for the 1s $\rightarrow$ 3d transition in XANES. Therefore, the intensity of this transition in the UV−vis region is very low, compared to transitions in tetrahedral systems,[42] which is observed in Figure 7. This indicates that the two as-synthesized samples do not contain any tetrahedral cobalt, although some octahedral cobalt is present. Because the average coordination number of these samples is ∼5 (see Table 3), some of the cobalt may be located in different types of distorted environments inside the amorphous framework.

Also note that most of the spectra in Figure 7 also contain an indication of a broad peak above 30 000 cm^{-1}, and similar peaks have also been observed by other authors.[6,22,27] The cause of these peaks are less understood than the peaks in the visible
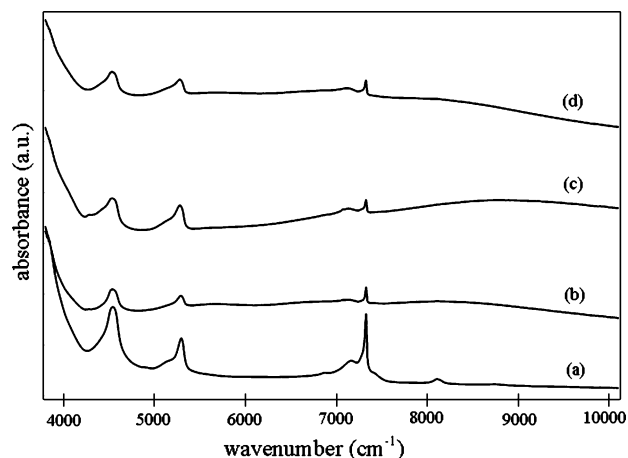

Figure 8. Near-infrared (NIR) spectra of (a) sample MCM-41, (b) sample OP-41-A, (c) sample OP-41-B, and (d) sample G-41.

region, but may be due to charge-transfer transitions or absorption by the porous matrix.

Near-Infrared and Infrared Spectroscopy. Electronic transitions in metal complexes are also caused by photons with wavelengths in the NIR region of the electromagnetic spectrum. For tetrahedral Co(II) complexes, the $^4A_2 \rightarrow {}^4T_1(F)$ transition occurs in the region between 5000 and 9000 cm^{-1},[16,43] and this transition has been observed for tetrahedral Co(II) in microporous materials.[4,6,11,16] Figure 8 shows the NIR spectra of calcined samples OP-41-A and OP-41-B and sample G-41. The spectrum of MCM-41 has also been included for comparison. From the figure, it can be seen that the $^4A_2 \rightarrow {}^4T_1(F)$ transition is not as readily observed as the $^4A_2 \rightarrow {}^4T_1(P)$ triplet in the UV−vis region. However, the spectra of samples G-41 and OP-41-A contain a broad peak with low intensity between 5000 and 9000 cm^{-1} that is not observed for sample MCM-41, which may be attributed to this transition. The spectrum of sample OP-41-B also contains such a broad peak, but this peak is shifted toward higher wavenumbers, possibly because of the distorted local environment of cobalt in this sample. Vinu et al. investigated Co−SBA-1 with UV−vis−NIR spectroscopy, and they did not observe this $^4A_2 \rightarrow {}^4T_1(F)$ transition in the NIR region at all.[22] However, they attributed this to a possible trigonal pyramidal symmetry around cobalt in the framework. This is probably not the case for the samples in the present study, because the EXAFS analyses showed that the coordination number of cobalt is 4 and that the XANES and UV−vis results indicate tetrahedral coordination. Therefore, the $^4A_2 \rightarrow {}^4T_1(P)$ transition for tetrahedral Co(II) seems to be perhaps more difficult to observe for cobalt-containing mesoporous materials than for cobalt-containing microporous materials.

However, spectroscopy in the infrared region is usually used to study vibrational modes and identify the nature of functional surface groups such as silanol. Figure 8 shows that all the cobalt-containing samples contain silanol groups. The peak at ∼4530 cm^{-1} can be assigned to a combination of the stretching and deformation modes of silanol groups ($\nu_{OH} + \delta_{OH}$), and the peak at ∼7320 cm^{-1} can be assigned to the first overtone of the stretching mode ($2\nu_{OH}$),[44−46] although the intensities of these peaks are significantly lower than for the pure siliceous sample MCM-41. This decrease in the number of silanol groups is due to the presence of cobalt at the surface and such a similar decrease has also been observed by Suvanto et al., who deposited cobalt onto the surface of sample MCM-41 via a gas-phase method.[21]

A comparison of the number of silanol groups is more suitable by comparing the intensities of the main Si−OH stretching mode

Cobalt-Containing Mesoporous Materials

J. Phys. Chem. B, Vol. 110, No. 11, 2006 **5393**

TABLE 4: Intensity of the Main Silanol Peak and Estimation of Surface Acidity after Adsorption of Pyridine for Samples MCM-41, OP-41-A, OP-41-B, and G-41

sample	absorption intensity[a]	acidity (mmol/g)[b]
MCM-41	0.561	0.0073
OP-41-A	0.480	0.067
OP-41-B	0.507	0.031
G-41	0.446	0.082

[a] Intensity of absorption peak at ∼3745 cm^{-1}. [b] Estimated by methods reported in the literature,[34,35] as described in the experimental part.
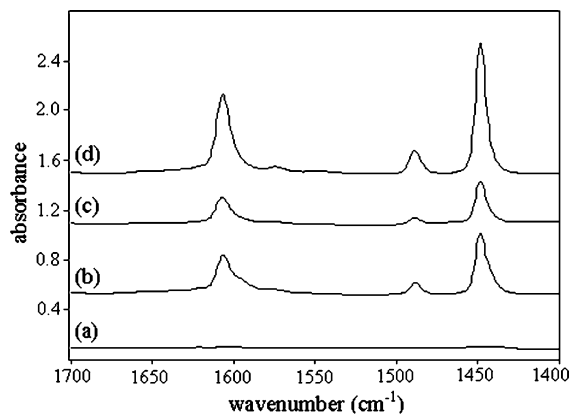
Figure 9. Difference IR spectra after the adsorption of pyridine for (a) sample MCM-41, (b) sample OP-41-A, (c) sample OP-41-B, and (d) sample G-41.

at ∼3745 cm^{-1} in the mid-IR region,[44] which was observed for all samples (not shown). Table 4 lists the intensities of this peak collected after activation in a vacuum, and the highest intensity is observed for the pure siliceous sample MCM-41, as expected. Compared to sample MCM-41, there is a significant intensity decrease for both the OP samples, which shows that the incorporation of cobalt into the framework affects the amount of surface silanol groups. However, the lowest intensity of the silanol band at ∼3745 cm^{-1} is observed for sample G-41. In this sample, all the cobalt is located at the silica surface and is not distributed evenly throughout the framework as for the two OP samples. Therefore, this presence of cobalt at the surface greatly affects the number of free silanol groups, which is reflected in the significant intensity decrease, compared to sample MCM-41 (see Table 4). It is also important to note that the spectra of the activated samples OP-41-A and OP-41-B contained a new feature that is located at ∼3624 cm^{-1} (not shown). This peak can be assigned to vibrations of the Co−OH group[47] and was only observed for the framework incorporated samples.

The incorporation of metals such as aluminum into mesoporous materials have been reported to create acid sites of both Brönsted and Lewis types.[34,48,49] The adsorption of pyridine followed by collection of IR data is often used to detect and identify different types of acid sites,[50] because of the characteristic vibrational modes of adsorbed pyridine. Figure 9 shows the difference IR spectra collected for samples MCM-41, OP-41-A, OP-41-B, and G-41 after the adsorption of pyridine at 150 °C with a partial pressure of 10^{-2} mbar. For the pure siliceous sample, there is no significant difference in the IR spectra before and after the pyridine adsorption. A very small band can be observed at ∼1449 cm^{-1} however, which indicates the presence of Lewis acid sites.[50,51] The difference spectra of the three cobalt-containing samples contain clearly visible peaks at 1449, 1490, and 1608 cm^{-1}, which may all be assigned to

vibrational modes of pyridine adsorbed on Lewis acid sites.[50,51] For pyridine adsorbed at Brönsted acid sites, such characteristic vibrational modes can be found at ∼1550 cm^{-1}, and there are no visible peaks observed in the difference spectra for any of the samples (see Figure 9). Therefore, all the cobalt-containing samples studied here contain Lewis acid sites and no Brönsted acid sites.

The calculated acidities for the different samples are listed in Table 4. There is a major difference in acidity between the two OP samples, where sample OP-41-A has a significantly higher concentration of acid sites than sample OP-41-B. We suggest that this difference is attributed to the difference in the amount of tetrahedral cobalt in these samples, as observed by XANES and UV−vis spectroscopy in Figures 6 and 7, respectively. Therefore, it seems as if the amount of tetrahedral cobalt in the sample affects the concentration of acid sites. The highest acidity of all the samples is observed for sample G-41, which also contains a large amount of tetrahedral cobalt (see Figures 6 and 7). However, in contrast to sample OP-41-A, all the tetrahedral cobalt in sample G-41 is located at the surface, not evenly distributed throughout the sample. Therefore, the higher acidity of sample G-41 is suggested to be due to the high amount of tetrahedral cobalt at the surface, which indicates that the Lewis acid sites are located at these tetrahedral cobalt sites.

4. Conclusions

In this paper, cobalt-containing mesoporous materials have been characterized by the some of the most common spectroscopic techniques. Transmission electron microscopy/energy-dispersive X-ray spectroscopy (TEM/EDS) analyses have revealed that tetraethyl orthosilicate (TEOS) may be unsuitable as a silicon source during the synthesis of these types of materials. Through careful extended X-ray absorption fine structure (EXAFS) analyses, it is possible to identify and distinguish between surface-bound cobalt and framework-incorporated cobalt. Such direct information may not be obtained via ultraviolet−visible (UV−vis) spectroscopy. Information about the coordination symmetry of cobalt may be obtained by both X-ray absorption near edge spectroscopy (XANES) and UV−vis spectroscopy, and there is good agreement between the results from these methods. Tetrahedral cobalt at the surface has been observed to create Lewis acid sites. The results from the various methods complete each other and, when considered together, the results provide a thorough understanding of the properties and local environment of cobalt in this type of material.

References and Notes

(1) Shelef, M. *Chem. Rev.* **1995**, *95*, 209.
(2) Traa, Y.; Burger, B.; Weitkamp, J. *Microporous Mesoporous Mater.* **1999**, *30*, 3.
(3) Wichterlová, B. *Top. Catal.* **2004**, *28*, 131.
(4) Uytterhoeven, M. G.; Schoonheydt, R. A. *Microporous Mater.* **1994**, *3*, 265.
(5) Decedek, J.; Wichterlová, B. *J. Phys. Chem. B* **1999**, *103*, 1462.
(6) Sponer, J.; Cejka, J.; Decedek, J.; Wichterlová, B. *Microporous Mesoporous Mater.* **2000**, *37*, 117.

(7) Dalconi, M. C.; Alberti, A.; Cruciani, G.; Ciambelli, P.; Fonda, E. *Microporous Mesoporous Mater.* **2003**, *62*, 191.

(8) Thomson, S.; Howe, R. *Phys. Chem. Chem. Phys.* **1999**, *1*, 615.

(9) de Bont, P. W.; Vissenberg, M. J.; de Beer, H. J.; van Veen, J. A. R.; van Santen, R. A.; van der Kraan, A. M. *J. Phys. Chem. B* **1998**, *102*, 5876.

(10) Park, J.-H.; Park, C. H.; Nam, I.-S. *Appl. Catal., A* **2004**, *277*, 271.

(11) de Montes, C. A.; de Villa, P. A. L.; Ramirez-Corredores, M. M. *Appl. Catal., A* **2000**, *197*, 151.

(12) Sankar, G.; Thomas, J. M.; Chen, J.; Wright, P. A.; Barrett, P. A.; Greaves, G. N.; Catlow, C. R. A. *Nucl. Instrum. Method B* **1995**, *97*, 37.

(13) Barrett, P. A.; Sankar, G.; Catlow, C. R. A.; Thomas, J. M. *J. Phys. Chem.* **1996**, *100*, 8977.

(14) Rajic, N.; Ristic, A.; Tuel, A.; Kaucic, V. *Zeolites* **1997**, *18*, 115.

(15) Moen, A.; Nicholson, D. G.; Rønning, M.; Lamble, G. M.; Lee, J.-F.; Emerich, H. *J. Chem. Soc., Faraday Trans.* **1997**, *93*, 4071.

(16) Verberckmoes, A. A.; Weckhuysen, B. M.; Schoonheydt, R. A. *Microporous Mesoporous Mater.* **1998**, *22*, 165.

(17) Chao, K. J.; Wei, A. C.; Wu, H. C.; Lee, J. F. *Catal. Today* **1999**, *49*, 277.

(18) Kresge, C. T.; Leonowicz, M. E.; Roth, W. J.; Vartuli, J. C.; Beck, J. S. *Nature* **1992**, *359*, 710.

(19) Beck, J. S.; Vartuli, J. C.; Roth, W. J.; Leonowicz, M. E.; Kresge, C. T.; Schmitt, K. D.; Chu, C. T.-W.; Olson, D. H.; Sheppard, E. W.; McCullen, S. B.; Higgins, J. B.; Schlenker, J. L. *J. Am. Chem. Soc.* **1992**, *114*, 10834.

(20) Jentys, A.; Pham, N. H.; Vinek, H.; Englisch, M.; Lercher, J. A. *Microporous Mater.* **1996**, *6*, 13.

(21) Suvanto, S.; Hukkamäki, J.; Pakkanen, T. T.; Pakkanen, T. A. *Langmuir* **2000**, *16*, 4109.

(22) Vinu, A.; Dedecek, J.; Murugesan, V.; Hartmann, M. *Chem. Mater.* **2002**, *14*, 2433.

(23) Lim, S.; Ciuparu, D.; Pak, C.; Dobek, F.; Chen, Y.; Harding, D.; Pfefferle, L.; Haller, G. *J. Phys. Chem. B* **2003**, *107*, 11048.

(24) Haskouri, J. E.; Cabrera, S.; Gomez-Garcia, C. J.; Guillem, C.; LaTorre, J.; Beltran, D.; Marcos, M. D.; Amoros, P. *Chem. Mater.* **2004**, *16*, 2805.

(25) Vrålstad, T.; Øye, G.; Rønning, M.; Glomm, W. R.; Stöcker, M.; Sjöblom, J. *Microporous Mesoporous Mater.* **2005**, *80*, 291.

(26) Béland, F.; Badei, A.-R.; Rønning, M.; Nicholson, D. G.; Bonneviot, L. *Phys. Chem. Chem. Phys.* **1999**, *1*, 605.

(27) Vinu, A.; Hartmann, M. *Chem. Lett.* **2004**, *33*, 588.

(28) Jentys, A.; Pham, N. H.; Vinek, H.; Englisch, M.; Lercher, J. A. *Catal. Today* **1998**, *39*, 311.

(29) Lim, S.; Ciuparu, D.; Chen, Y.; Yang, Y.; Pfefferle, L.; Haller, G. *J. Phys. Chem. B* **2005**, *109*, 2285.

(30) Vrålstad, T.; Øye, G.; Stöcker, M.; Sjöblom, J. Submitted.

(31) Vrålstad, T.; Øye, G.; Sjöblom, J.; Stöcker, M. *J. Dispersion Sci. Technol.*, in press.

(32) Ressler, T. *J. Synchrotron. Radiat.* **2004**, *5*, 118.

(33) Binsted, N. *EXCURVE98*; Daresbury Laboratory: Warrington, Cheshire, U.K., 1998.

(34) Jentys, A.; Kleestorfer, K.; Vinek, H. *Microporous Mesoporous Mater.* **1999**, *27*, 321.

(35) Emeis, C. A. *J. Catal.* **1993**, *141*, 347.

(36) Teo, B. K. *EXAFS: Basic Principles and Data Analysis*; Springer−Verlag: Berlin, Germany, 1986.

(37) Zhao, D.; Feng, J.; Huo, Q.; Melosh, N.; Fredrickson, G. H.; Chmelka, B. F.; Stucky, G. D. *Science* **1998**, *279*, 548.

(38) Moen, A.; Nicholson, D. G.; Rønning, M.; Emerich, H. *J. Mater. Chem.* **1998**, *8*, 2533.

(39) Rønning, M.; Nicholson, D. G.; Holmen, A. *Catal. Lett.* **2001**, *72*, 141.

(40) Fernández-Garcia, M. *Catal. Rev.* **2002**, *44*, 59.

(41) Holleman, A. F.; Wiberg, E. *Inorganic Chemistry*; Academic Press: New York, 2001.

(42) Kettle, S. F. A. *Physical Inorganic Chemistry−A Coordination Chemistry Approach*; Oxford University Press: New York, 1998.

(43) Cotton, F. A.; Wilkinson, G.; Murillo, C. A.; Bochmann, M. *Advanced Inorganic Chemistry*; 6th Edition; Wiley: New York, 1999.

(44) Morrow, B. A.; McFarlan, A. J. *J. Phys. Chem.* **1992**, *96*, 1395.

(45) Peña, M. L.; Dellarocca, V.; Rey, F.; Corma, A.; Coluccia, S.; Marchese, L. *Microporous Mesoporous Mater.* **2001**, *44−45*, 345.

(46) Gianotti, E.; Dellarocca, V.; Marchese, L.; Martra, G.; Coluccia, S.; Maschmeyer, T. *Phys. Chem. Chem. Phys.* **2002**, *4*, 6109.

(47) Liang, Y.-Y.; Cao, L.; Kong, L.-B.; Li, H.-L. *J. Power Sources* **2004**, *136*, 197.

(48) Hunger, M.; Schenk, U.; Breuninger, M.; Gläser, R.; Weitkamp, J. *Microporous Mesoporous Mater.* **1999**, *27*, 261.

(49) Collart, O.; Cool, P.; Van Der Voort, P.; Meynen, V.; Vansant, E. F.; Houthoofd, K.; Grobet, P. J.; Lebedev, O. I.; Van Tendeloo, G. *J. Phys. Chem. B* **2004**, *108*, 13905.

(50) Jacobs, P. A. In *Characterization of Heterogeneous Catalysts*; Delannay, F., Ed.; Marcel Dekker: New York, 1984.

(51) Ward, J. W. *J. Catal.* **1967**, *9*, 225.